RSC Advances

PAPER

View Article Online
View Journal | View Issue

Cite this: *RSC Adv.*, 2023, **13**, 15366

Green emission from trivalent cerium doped $LaAlO_3$/MgO nano-composite for photonic and latent finger printing applications

Ashima Makhija,[a] Anjli Sharma,[a] Sajjan Dahiya,[a] Nisha Deopa,[b] Rajesh Malik,[c] R. Punia *[a] and A. S. Maan[a]

A series of Ce^{3+} doped $La_{1-x}Ce_xAlO_3$/MgO (x = 0, 0.7, 0.9, 1.0 and 2.0 mol%) nano-composites have successfully been synthesized employing the Pechini sol–gel method. XRD profiles assisted with Rietveld refinement results manifested the rhombohedral/face-centered structures of the two phases of the generated composite. Thermogravimetric results corroborate the crystallization temperature of the compound to be 900 °C, that further remains stable up to 1200 °C. Materials have been found to be wide band gap semi-conductors having E_g in the range of 5.5–5.8 eV. Photoluminescence studies reveal their green emission under UV excitation of 272 nm. Application of Dexter's theory and Burshtein model to PL and TRPL profiles, respectively reveals the q–q multipole interlinkages to be the viable cause of concentration quenching beyond optimum concentration of 0.9 mol%. Shifting of the energy transfer route from cross-relaxation to migration assisted mechanism with Ce^{3+} concentration has also been investigated. Other luminescence based parameters such as energy transfer probabilities, efficiencies, CIE and CCT have also been found to be in an admirable range. From the aforesaid results, it was observed that the optimized nano-composite (*i.e.* $La_{1-x}Ce_xAlO_3$/MgO (x = 0.9 mol%)) can also be utilized for latent finger-printing (LFP) application that evinces its versatility for photonic as well as imaging applications.

Received 30th March 2023
Accepted 15th May 2023

DOI: 10.1039/d3ra02078a

rsc.li/rsc-advances

1. Introduction

Solid state lighting technology has advocated a great revolution due to the development of pc-w-LEDs for their ubiquitous applications and their proficient features including low-power usage, robustness, high luminosity, good fidelity, long life-span (>100 000 h), fast switching, *etc.*[1,2] Current mainstream patterns of developing w-LEDs involve either the encapsulation of blue LEDs with yellow emitting phosphor YAG:Ce^{3+} or pumping trichromatic blue, green, red (BRG) phosphors with UV light.[3,4] However, the first strategy suffers due to high CCT, low color rendering index (R_a < 80), halo-effect, thermal quenching, *etc.* In the later category, the commercially used tri-color phosphor materials are $BaMgAl_{10}O_{17}:Eu^{2+}$ for blue, ZnS:(Cu^+, Al^+) for green and $Y_2O_2S:Eu^{3+}$ for red emission. But the thermal and chemical stability of sulphide phosphors is very low. Moreover, they are also prone to emit sulphur gas into the atmosphere, thus are toxic.[5] Resultantly, myriad research is being done in search of a novel phosphor matrix possessing efficient characteristics. Recent years have witnessed the trend of developing and exploring nano-composite materials to solve innumerous inexorable problems including nano-phosphor composite materials.[6,7] However, the rate of research on composite phosphors is much less than the research being done on crystalline and glassy materials.

This urged the authors to generate a fresh and noble nano-composite material that is stable, viable and environment friendly; which has high band gap, low phonon frequency as required for acting as an efficient host matrix when doped with a suitable activator. In this regard, a nano-composite of $LaAlO_3$ (LAO) and MgO (MO) has been synthesized since both have high band-gaps in the range of 5.3–5.8 eV and 5.8–6.3 eV respectively.[8–10] Additionally, oxides are highly stable and thus are devoid of afore-mentioned snags.[11] Concerning activator, rare-earth elements are mostly preferred for their sharp spectra. Amongst several rare-earths, Ce^{3+} is a well-known paradigm of it for its abundance in nature and promising spectral emissions in green and blue region of visible spectrum due to its allowed f–d transitions. Therefore, has been vastly explored in several host matrices such as, $Y_3Al_5O_{12}$, $CaY_2HfGa(AlO_4)$, $CaSc_2O_4$, *etc.*, for green color luminescence and $Sr_2Al_2SiO_7$, $Ba_3La_2(BO_3)_4$, $SrZrSi_2O_7$, CaZrO3 *etc.*, for blue colour emission for its innumerable applications in display devices, wLEDs, scintillators, laser amplifiers in fibre-optics communications, solar cells, *etc.*[12–18] Individually Ce^{3+} doped LAO have been studied earlier and have shown excellent luminescence.[19–21] This motivated the

[a]Department of Physics, Maharshi Dayanand University, Rohtak 124001, India. E-mail: rajeshpoonia13@gmail.com
[b]Department of Physics, Chaudhary Ranbir Singh University, Jind 126102, India
[c]Department of Chemistry, Maharshi Dayanand University, Rohtak 124001, India

authors to synthesize and investigate luminescence in novel Ce^{3+} doped nano-composite $LaAlO_3$/MgO material.

Besides aforementioned photonic applications, phosphors are widely being explored for Latent Finger Printing (LFP) applications. It an effective anti-counterfeiting technique for prevention of circulation and detection of forged banknotes, currency, certificates, *etc.* along with investigations of crime scene.[22,23] In this, luminescent material is deposited on latent fingerprints and then visualized under suitable UV lamp. Each fingerprint pattern features can be classified into 3 levels based on the minuteness of it. Level 1 being the coarse details and level 3 showing the finest details of the pattern that help identify the criminal. Efforts have been made to prepare effective phosphor powder that can help identify fingerprints from each kind of surface and up to core level 3 of pattern.[24,25]

The prime aim of this article is to study the luminescence of Ce^{3+} doped nano-composites $La_{1-x}Ce_xAlO_3$/MgO and its advantage over individually Ce^{3+} doped LAO has also been discussed.

2. Experimental

2.1 Materials and synthesis of nanocomposite

All the precursor salts, namely, $La(NO_3)_3 \cdot 6H_2O$ (purity 99%), $Al(NO_3)_3 \cdot 9H_2O$ (purity 98.5%), $Mg(NO_3)_2 \cdot 6H_2O$ (purity 99.5%), $Ce(NO_3)_3 \cdot 6H_2O$ (purity 99%) (all procured from Hi-media, AR grade) and citric acid (purity 98%) (Merk, AR grade) were used as obtained without any further purification.

Pristine as well as Ce doped nanocomposites $La_{1-x}Ce_xAlO_3$/MgO ($x = 0$, 0.3, 0.5, 0.7, 0.9, 1.0 and 2.0 mol%) were prepared using citrate assisted Pechini sol–gel method in single step (Fig. 1). For this, initially stoichiometric ratios of all the metal salts were dissolved in minimum amount of distilled water at room temperature. Subsequently, citric acid with respect to metal ion in the ratio 2 : 1 (CA : M) was added and stirred vigorously at 80 °C until gelation occurs. Thereafter, temperature was raised to 120 °C that lead to auto-combustion followed by frothing and fuming resulting in white coloured wet-sponges that turn into dry brown sponges (as-prepared dried xerogel) within a few minutes. The resultant is subsequently powdered using mortar pestle and then sintered at different calcination temperatures for 3 h over the range of 650 °C–1200 °C for further characterizations. Out of these dopant concentrations, it was observed that $x = 0.3$ and 0.5 mol% shows negligible luminescence. Observable luminescence began with $x = 0.7$ mol% that reached its maxima for $x = 0.9$ mol% and decreased thereafter for increasing Ce^{3+} concentrations. Therefore, $x = 0.7$, 0.9, 1.0 and 2.0 mol% were studied in detail.

Pellet of undoped nanocomposite for *P–E* curve tracing was prepared by adding 5 drops of hot water soluble PVA@3 wt% to the sintered powder and mixed thoroughly. The prepared sticky powder was then moulded into pellet using 7 mm dye. Prepared pellet was again sintered at 1200 °C for 3 h in tubular furnace to remove the traces of added PVP.

2.2 Methodology

The thermal analysis were performed using DSC-TG analyzer (TA instruments/Q600-SDT) from room temperature to 1200 °C at the ramp rate of 5 °C min^{-1} in the presence of oxygen gas and the diffraction patterns were recorded by Rigaku/miniflex-600 table top X-ray Diffractometer employing Cu-Kα (1.5406 Å) X-ray radiation source over the 2θ range of (10°–80°) with the scan rate of 1° min^{-1}. XRD profile were Rietveld refined using FullProf program and crystal structures were visualized utilizing Vesta software program.[26–28] *P–E* hysteresis curves were traced using Marine India's Highend PE ferroelectric test system for electric fields in the range of 25–100 kV cm^{-1}. UV-DRS spectroscopy was done using Shimadzu-3600 plus UV-spectrophotometer in the wavelength range 200–800 nm in reflectance mode. Steady state PL spectroscopy was performed using Horiba instruments Fluorescence spectrophotometer (FL3C-21) assisted with double grating monochromator and Xe-lamp in the range 380–750 nm for emission spectra and 250–420 nm for excitation spectra where as time resolved PL spectroscopy (TRPL) was carried out using FL-spectrophotometer by HITACHI F-7000 using Xe lamp operated at 400 V. Imaging of fingerprints and samples were done using UV Fluorescence analysis cabinet equipped with short range UV source of wavelength 254 nm operated at 60 Hz, 220 V.

2.3 Latent fingerprint visualisation

To collect finger-prints of donor, his hands were thoroughly washed with soap and water followed by drying in normal air. Then his thumb was gently pressed on donor's forehead and fingerprint was collected on a glass-slide. This latent fingerprint was then produced using optimized phosphor, *via* powder dusting method. Extra powder was removed carefully by using soft brush. Then, the pattern was visualized under short range UV lamp (254 nm) cabinet and photographed.

3. Results and discussion

3.1 Thermal analysis

Fig. 2 depicts the TGA and DSC thermograms of unsintered pristine powdered xerogel. The TGA shows a total weight loss of 88.41% at 900 °C and remains constant thereafter upto 1200 °C. The initial weightloss of 8.7% around 200 °C may be attributed to desorption of adsorbed water vapours which is confirmed by the presence of an endothermic peak. Then the subsequent weightloss of approximately 85.34% between 200–550 °C may be due to decomposition of citric acid complexes, crystallization of MO phase and release of nitrous and carbonaceous gases, affirmed by the presence of two exothermic peaks at 426 °C and 507 °C in this region. Final weightloss between 730–900 °C may be attributed to the burning of residual organic complexes and crystallization of LAO. The corresponding DSC curve shows an endothermic dip accompanied with an exothermic process at around 850 °C helps identify the calcination temperature to be 900 °C.[29–31] Above this a stable phase is obtained. Involved chemical reaction for the whole process follows the given reaction (1) for which total weightloss is calculated to be 87.84% that matches well with the experimental observations (*i.e.* 88.41%).

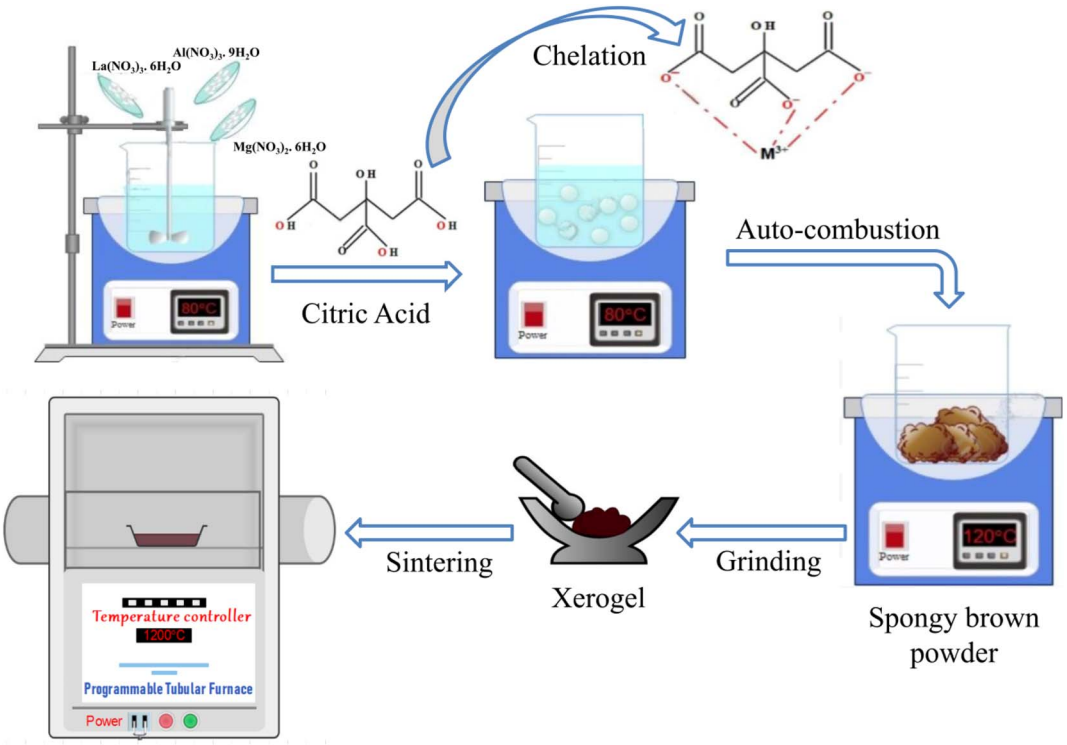

Fig. 1 Schematics of composite synthesis using Pechini sol–gel method.

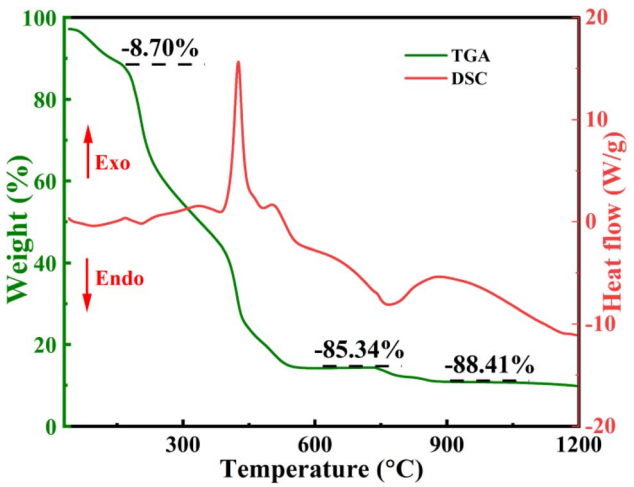

Fig. 2 Differential Scanning Calorimetry (DSC) and Thermo-Gravimetric Analysis (TGA) curves of pristine powder $LaAlO_3$/MgO.

$$Mg(NO_3)_3\cdot 6H_2O + Al(NO_3)_3\cdot 6H_2O + La(NO_3)_3\cdot 9H_2O + 4C_6H_8O_7 + 8O_2 \rightarrow LaAlO_3 + MgO + 24CO_2 + 4N_2 + 37H_2O \quad (1)$$

3.2 Structural analysis

For scrutinizing the calcination temperature, sintering temperature and the crystal phase of the composite so formed, the room temperature X-ray Diffraction (XRD) patterns of unsintered xerogel and calcined powders sintered at different temperatures were recorded and are indicated in Fig. 3(a). For xerogel, pattern is amorphous with 2 humps indicating the presence of 2 phases that have not yet crystallized. For calcined powder sintered at 650 °C, peaks for both the phases start to appear whose sharpness as well as intensities increases with the rise in temperature indicating the improvement in crystallinity.[29] The presence of an amorphous hump around 28°–30° is because of organic residues which reduce with the elevating temperature. Apparently, this hump is convoluted with lanthanum oxide peak at 28.936° at 800 °C.[32] At 900 °C, all these supplementary peaks vanish stipulating the calcination completion and pure crystalline phase is obtained, correlating with the DSC-TGA data. At 1200 °C, peaks become narrower and sharper as a result of larger crystallite size and better crystallinity of the composite so formed.

The diffraction profile of the nano-composite so formed can be ascribed to the reference JCPDS card #87-0653 for MO (space group: $Fm\bar{3}m$ (225)) and for LAO it matches well with card #82-0478 (space group: $R\bar{3}c$ (167)) as well as with card #31-0022 (space group: $Pm3m$ (221)) since both the cards possess peaks at same positions with different miller indices. S. Kozuka *et al.*, I. S. Silveira *et al.*, D. Singh *et al.*, M. Beheshti *et al.* have reported it to be rhombohedral whereas authors such as P. Kumar *et al.*, E. B. Shaik *et al.* and P. Ankoji *et al.* have reported it to be belonging to later space group having primitive cubic structure.[32–38] LAO is known to transit from rhombohedral to primitive structure around 800 K.[39] So, at room temperature its XRD should be ascribed to rhombohedral space group. To ascertain the same, Rietveld refinement of diffractograms using

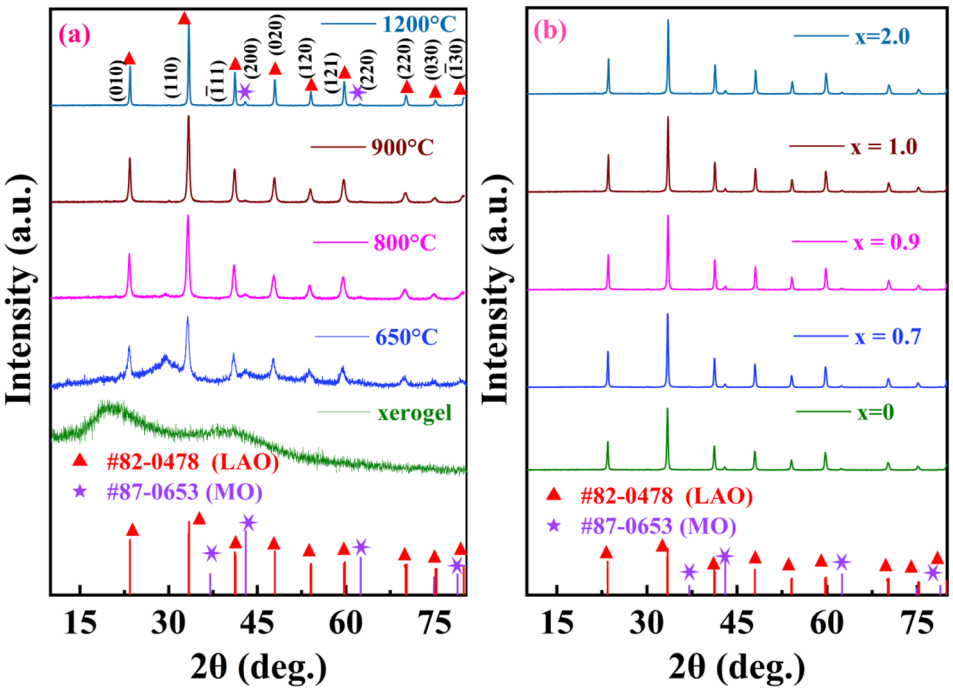

Fig. 3 X-ray Diffraction (XRD) pattern of $La_{1-x}Ce_xAlO_3$/MgO (a) for $x = 0$ unsintered xerogel powder, powder sintered at 650 °C, 800 °C, 900 °C and 1200 °C along with reference JCPDS and (b) $x = 0$, 0.7, 0.9, 1.0 and 2.0 mol%.

both the space groups have been performed and displayed in Fig. 4(a) and (b). Chi-square and *R*-factors for both the models were found to be in acceptable range, with chi-square value being lower for the rhombohedral model. To support this experimentally, polarization *vs.* electric field (*P*–*E*) hysteresis curve tracing experiment at room temperature had been conducted using pallet of the nano-composite so formed. In this, an oscillating electric field at a constant potential difference is applied across the crystal that induces spontaneous polarization within it thus, material exhibits hysteresis loop. As a matter of fact, cubically symmetric crystals can never be polarized because centre of charges for both the anion and cation coincides under given symmetric conditions and will never be separated for dipole formation whereas for non-cubic crystals such segregation of centre of charges may take place leading to dipole formation and hence resultant polarization.[40] Presence of hysteresis curve in Fig. 4(c) corroborates the fact that the material is non-cubic at room temperature. So the nano-composite so formed has crystallized into rhombohedral space group.

Fig. 3(b) also shows the diffraction patterns of Ce^{3+} doped nano-composites $La_{1-x}Ce_xAlO_3$/MgO (x = 0, 0.7, 0.9, 1.0, 2.0 mol%) sintered at 1200 °C which is analogous to the one observed for host matrix. The absence of any conspicuous peak indicates that Ce^{3+} ion has successfully been incorporated into the host matrix and has efficiently substituted the host cation. According to Hume–Rothery rules for substitutional solid solutions, maximum solubility occurs when host and dopant ions have similar ionic radii, valencies and electro-negativities.[41] Here, firstly replacement of Mg^{2+} by Ce^{3+} is ruled out based on the dissimilarities in all the aspects. For LAO, although both the host cations La^{3+} & Al^{3+} have analogous valencies to that of dopant Ce^{3+} but ionic radii and electro-negativity of Al^{3+} is considerably different. Quantitatively, if the differential radii percentage (Δr) is less than 30% only then the substitution is feasible, that is calculated by (2)

$$\Delta r = \frac{R_h(CN) - R_d(CN)}{R_h(CN)} \times 100 \quad (2)$$

where, R_h and R_d are ionic radii of host and dopant ions respectively for their corresponding coordination numbers (CN)[3]. In the present study, calculated values of Δr for substitution of Al^{3+} ($r = 0.5375$ Å, CN = 6) and La^{3+} ($r = 1.36$ Å, CN = 12) by Ce^{3+} ($r = 1.01$ Å, CN = 6; $r = 1.34$ Å, CN = 12) are 87.90% and 1.47% respectively. So, the substitution of former is ruled out and later is validated.

The nano-composite samples $La_{1-x}Ce_xAlO_3$/MgO ($x = 0$ and 0.9 mol%) were sintered in the range of 900 °C–1200 °C and its effect on crystallite size was investigated. By employing Debye–Scherrer given by (3) as well as by Williamsons–Hall (W–H) method given as (4),

$$D = \frac{k\lambda}{\beta \cos\theta} \quad (3)$$

$$\beta \cos\theta = \frac{k\lambda}{D} + 4\varepsilon \sin\theta \quad (4)$$

where, D = crystallite size, β = full width half maxima of peaks, θ = Bragg's angle in deg., λ = 1.54 Å, k = 0.91 (Schherer's constant) and ε = strain produced.[42,43] From (4), plot of $\beta \cos\theta$ *vs.* 4 sin θ gives straight line with slope of line equating to strain

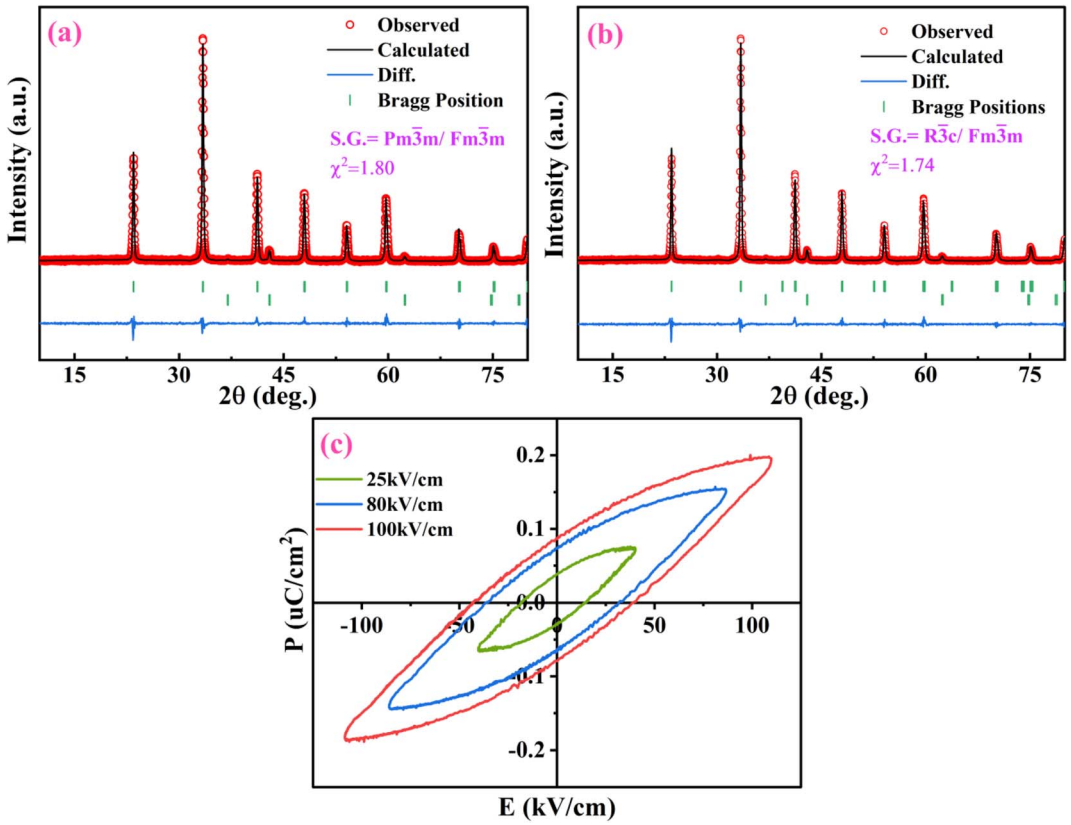

Fig. 4 Rietveld-refinement plot of $LaAlO_3$/MgO corresponding to space group (a) $Pm\bar{3}m/Fm\bar{3}m$, (b) $R\bar{3}c/Fm\bar{3}m$ and (c) polarization *vs.* electric field (*P*–*E*) hysteresis curve.

and reciprocal of intercept being propotional to *D*. Table 1 summarizes the calculated crystallite sizes and strains employing both the methods for all the samples. Fig. 5 depicts such W–H plot for $La_{1-x}Ce_xAlO_3$/MgO ($x = 0.7$ mol%). Here, it is worth noting that W–H method gives larger '*D*' because it helps eliminate strain-induced broadening, thus giving accurate '*D*'. From the perusal of data, it is observed that as sintering temperature rises, '*D*' increases and '*ε*' reduces for the both doped and undoped sample corroborating grain growth and better structure formation.[44] For doped samples all sintered at 1200 °C, as the dopant concentration increases, '*ε*' reduces because the dopant Ce^{3+} radii is smaller than the substituted La^{3+} radii causing lesser tensile stress.[45]

Rietveld refinement of the samples were performed and comparative results such as reliability factors χ^2, R_p, R_{wp}, R_{exp}, goodness of fit (GOF); and refined parameters such as phase percentages, lattice parameters (*a*), densities (*δ*), atomic fractional co-ordinates and occupancies of all the doped/undoped

Table 1 Debye Scherrer and Williamson–Hall (W–H) results of $La_{1-x}Ce_xAlO_3$/MgO ($x = 0$, 0.7, 0.9, 1.0, 2.0 mol%) along with their sintering temperatures; *D* = crystallite size, *ε* = strain, χ^2, R^2 = fitness parameters

			Williamson–Hall			
x (mol%)	Sintering temp. (°C)	Debye Scherrer *D* (nm)	χ^2	R^2	*D* (nm)	*ε*
0	900	19.25189	1.521×10^{-6}	0.95206	43.53870	0.00372
	1000	23.76002	3.089×10^{-7}	0.97003	39.16050	0.00214
	1100	32.18536	7.902×10^{-9}	0.99795	59.65728	0.00172
	1200	33.07412	1.663×10^{-7}	0.96578	63.15072	0.00166
0.7	1200	33.01666	1.663×10^{-7}	0.96578	56.53008	0.00147
0.9	900	19.60934	5.195×10^{-7}	0.95706	30.27961	0.00231
	1000	22.68407	4.164×10^{-7}	0.94327	32.00790	0.00178
	1100	28.84360	1.598×10^{-7}	0.96945	44.22543	0.00153
	1200	33.16457	2.519×10^{-7}	0.93728	51.73232	0.00141
1.0	1200	33.97841	9.473×10^{-8}	0.94654	52.50734	0.00133
2.0	1200	34.79318	1.125×10^{-7}	0.93516	53.92100	0.00130

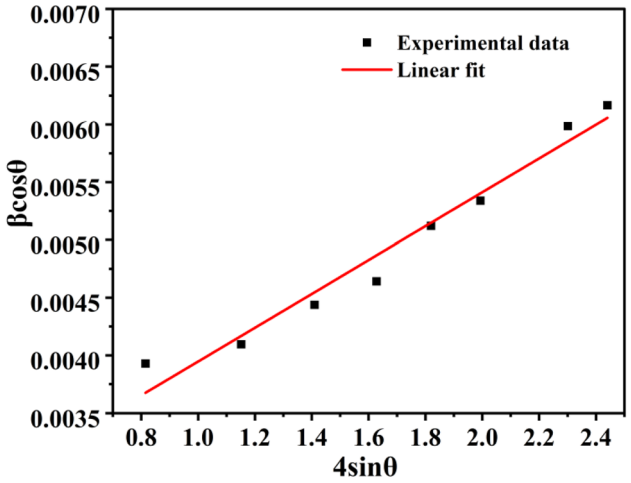

Fig. 5 Williamson–Hall (W–H) plot of $La_{1-x}Ce_xAlO_3$/MgO (x = 0.7 mol%).

nano-composites have been tabularized in Table 2 which confirms all the samples crystallize into afore-mentioned space groups. All the reliability factors are in acceptable range signifying excellent fitting. Noteworthy is, the lattice parameters and volume of the unit cell goes on decreasing when dopant concentration increases from 0.7 to 2 mol% which is in accord with the fact that dopant ion has lesser radii than the substituted ion. Fig. 6 shows the crystal structure of both the phases using Vesta software. In this surrounding co-ordination spheres of all the cations have been shown.

3.3 Photoluminescence (PL) spectroscopy

3.3.1 PLE spectra of doped/undoped nano-composite and its components. To investigate the luminescence characteristics of the doped/un-doped nano-composite so formed and its various individual components, PL spectroscopy was performed. Fig. 7(a) shows the PLE curves for various samples at the emission wavelength of 529 nm. It can be manifested from the figure that MO strongly absorbs before 290 nm, attributed to excitation of 3- and 4-fold co-ordinated O^{2-} anions at edges (F^+ center) and in corners (F center); and weak absorption band between 320–420 nm is due to charge transfer on surface states of MO.[46] LAO shows feeble absorption in the entire region, which may be due to surface defects formed during synthesis whereas $La_{1-y}Ce_yAlO_3$ (y = 0.9 mol%) shows characteristic cerium 2 band absorption around 298 nm and 367 nm.[21,47] Synthesized pristine nano-composite $LaAlO_3$/MgO shows little absorption around 268 nm, whereas Ce^{3+} doped nano-composite $La_{1-x}Ce_xAlO_3$/MgO (x = 0.9 mol%) absorbs strongly featuring two broad humps centered about 272 nm and 367 nm with former being the most intense. Significant difference in absorption of undoped and doped composite can also be inferred from the sharp decrement in reflectance of x = 0.9 mol% doped sample in the range 250–450 nm as indicated in inset of the Fig. 7(a). Bands for both the cerium doped samples can unambiguously be assigned to Ce^{3+} 4f → 5d transitions. Shift in absorption wavelength of doped composite as compared to doped LAO is may be due to variation in band gap of the synthesized nano-composite.

3.3.2 PL emission spectra of doped/undoped nano-composite and its components. The Fig. 7(b) depicts the PL emission spectra of doped/undoped nano-composite and its individual components in the range 380–750 nm at the excitation wavelength of 272 nm whereas its inset reflects the zoomed-in image of the same in the range 380–660 nm. Peaks after 675 nm are mainly due to defects formed, which are maximized for LAO.[47,48] These defects reduce after composite formation and further diminish for the doped nano-composites. In the inset, MO emits strongly before wavelength of 400 nm and then at 499 nm. These can be attributed to various F-centers, oxygen vacancies and surface charge transfers for initial rise and to transition $^3B_{1u}$ → ^1Ag for later increment whereas LAO shows almost no luminescence in the visible region, but a little in UV region at 422 nm.[48,49] However, the pristine composite formed out of these two *i.e.* $LaAlO_3$/MgO shows strong emission about 424 and 475 nm but this also lies considerably in the UV region. For Ce^{3+} doped $La_{1-y}Ce_yAlO_3$ (y = 0.9 mol%) and $La_{1-x}Ce_xAlO_3$/MgO (x = 0.9 mol%), luminescence for both lies in green region with the later being highly intense.[21] This justifies the efficient behavior of composite than its individual components.

3.3.3 Effect of sintering temperature on PL emission at fixed doping concentration. Effect of sintering temperature (900–1200 °C) on $La_{1-x}Ce_xAlO_3$/MgO (x = 0.9 mol%) has been represented in Fig. 8(a) in which there is a subsequent red shift as temperature rises because '*D*' increases with sintering temperature which decreases quantum confinement and hence reduces band gap.[44] Also, PL intensity initially decreases when temperature rises to 1000 °C, thereafter gradually intensifies with rise in temperature upto 1200 °C. This trend is due to change in crystallite size with temperature. As '*D*' increases with temperature, surface area decreases. Since PL is a surface phenomenon, therefore, its intensity reduces. Whereas, with increasing temperature, its crystallinity improves, dopant ion substitutes better into the host matrix and grain boundary effect reduces which leads to increment in PL.[50] Hence, former factor dominates initially and later dominates thereafter. Therefore, all the samples have been sintered at 1200 °C.

3.3.4 Effect of doping concentration on PL emission at fixed sintering temperature. Pl emission spectra for Ce^{3+} doped phosphors $La_{1-x}Ce_xAlO_3$/MgO (x = 0.7, 0.9, 1.0, 2.0 mol%) by monitoring excitation wavelength at 272 nm was recorded. As shown in Fig. 8(b) the emission spectra of all the phosphor samples are absolutely alike *i.e.* a broad band centered about 529 nm. These can be de-convoluted into 2 broad peaks situated at 508.26 nm and 561.92 nm with the energy difference of 1892 cm^{-1}, which is close to theoretical value of 2000 cm^{-1}, as depicted in Fig. 8(c).[51] These peaks arise due to 5d → $^2F_{5/2}$ and 5d → $^2F_{7/2}$ transitions as indicated in schematic energy diagram (Fig. 8(d)). Fig. 8(e) shows the relative PL intensities of all the doped phosphors for peak at 508.26 nm in which x = 0.9 mol% proves to be the optimum concentration to fabricate green emissive phosphor. Decrement of emission intensity beyond optimum concentration is ascribed to the phenomenon

Table 2 Detailed data of Rietveld refinement profiles of $La_{1-x}Ce_xAlO_3$/MgO (x = 0, 0.7, 0.9, 1.0, 2.0 mol%); χ^2 = reduced chi-square value; R_p, R_{wp}, R_{exp}, R_f = Bragg-R factors; GOF = goodness of fit; a, b, c = lattice parameters; V = volume; δ = density; E= element name; x, y, z = atomic fractional co-ordinates; occ. = occupancy

x (mol%)		0	0	0.7	0.9	1.0	2.0
χ^2		1.80	1.74	2.38	3.66	3.87	3.61
R_p		7.26	7.09	7.75	10.1	10.1	10.4
R_{wp}		9.49	9.29	10.6	13.0	11.1	13.7
R_{exp}		7.06	7.06	6.90	6.82	6.06	6.89
GOF		1.34	1.32	1.53	1.90	1.83	1.98
Phases	LAO	$Pm\bar{3}m$	$R\bar{3}c$	$R\bar{3}c$	$R\bar{3}c$	$R\bar{3}c$	$R\bar{3}c$
	MO	$Fm\bar{3}m$	$Fm\bar{3}m$	$Fm\bar{3}m$	$Fm\bar{3}m$	$Fm\bar{3}m$	$Fm\bar{3}m$
Phase (%)	LAO	85.45	85.95	85.87	85.80	85.76	85.96
	MO	14.55	14.05	14.13	15.20	14.24	14.04
Bragg-R	LAO	4.21	2.62	3.88	5.00	9.92	9.00
	MO	1.99	1.75	2.63	3.25	5.78	5.18
R_f	LAO	9.21	8.85	4.69	5.00	9.92	9.00
	MO	5.75	5.48	3.55	2.49	8.74	2.74
a (Å), b (Å), c (Å)	LAO	3.792299	5.36633	5.36033	5.35692	5.35547	5.35333
		—	—	—	—	—	—
		—	13.12054	13.10622	13.09854	13.09406	13.05155
	MO	4.210361	4.21004	4.20612	4.20494	4.20257	4.20154
		—	—	—	—	—	—
		—	—	—	—	—	—
V (Å^3)	LAO	54.539	327.218	326.131	325.225	324.831	323.922
	MO	74.638	74.620	74.412	74.321	74.268	74.170
δ (gm cc^{-1})	LAO	6.511	6.513	6.535	6.553	6.553	6.580
	MO	3.587	3.587	3.598	3.602	3.607	3.609
E; x, y, z; occ.	LAO	La^{3+}	La^{3+}	La^{3+}/Ce^{3+}	La^{3+}/Ce^{3+}	La^{3+}/Ce^{3+}	La^{3+}/Ce^{3+}
		0.5, 0.5, 0.5	0, 0, 0.25	0, 0, 0.25	0, 0, 0.25	0, 0, 0.25	0, 0, 0.25
		0.02083	0.16667	0.16550/0.00117	0.16517/0.00150	0.16500/0.00167	0.16334/0.00333
		Al^{3+}	Al^{3+}	Al^{3+}	Al^{3+}	Al^{3+}	Al^{3+}
		0, 0, 0	0, 0, 0	0, 0, 0	0, 0, 0	0, 0, 0	0, 0, 0
		0.02083	0.16667	0.16667	0.16667	0.16667	0.16667
		O^{2-}	O^{2-}	O^{2-}	O^{2-}	O^{2-}	O^{2-}
		0.5, 0, 0	0.51976, 0, 0.25	0.51953, 0, 0.25	0.51059, 0, 0.25	0.50092, 0, 0.25	0.50301, 0, 0.25
		0.06250	0.5	0.5	0.5	0.5	0.5
	MO	Mg^{2+}	Mg^{2+}	Mg^{2+}	Mg^{2+}	Mg^{2+}	Mg^{2+}
		0, 0, 0	0, 0, 0	0, 0, 0	0, 0, 0	0, 0, 0	0, 0, 0
		0.02083	0.02083	0.02083	0.02083	0.02083	0.02083
		O^{2-}	O^{2-}	O^{2-}	O^{2-}	O^{2-}	O^{2-}
		0.5, 0.5, 0.5	0.5, 0.5, 0.5	0.5, 0.5, 0.5	0.5, 0.5, 0.5	0.5, 0.5, 0.5	0.5, 0.5, 0.5
		0.02083	0.02083	0.02083	0.02083	0.02083	0.02083

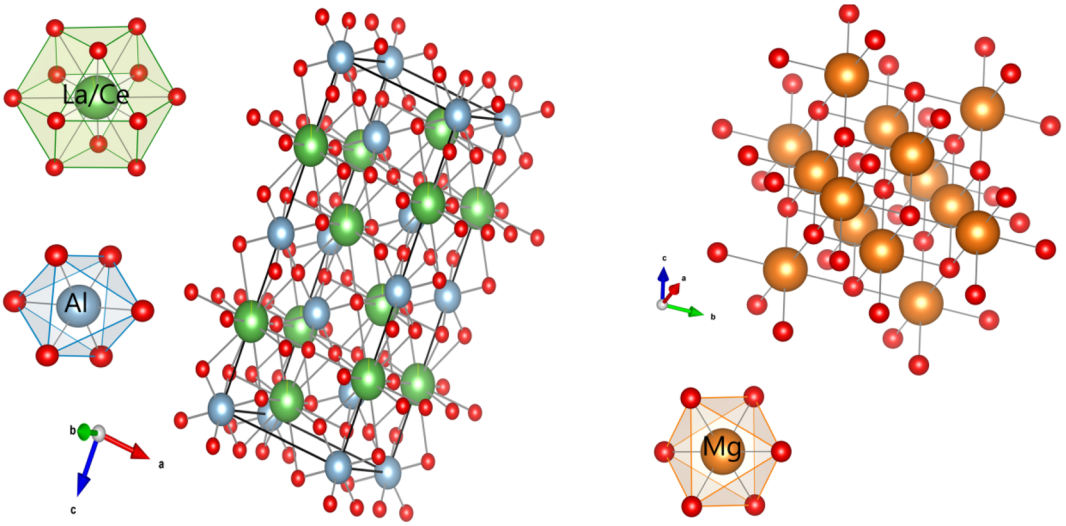

Fig. 6 Crystal structure of LAO and MO and cation co-ordinating spheres of Al^{3+}, La^{3+}/Ce^{3+} and Mg^{2+}.

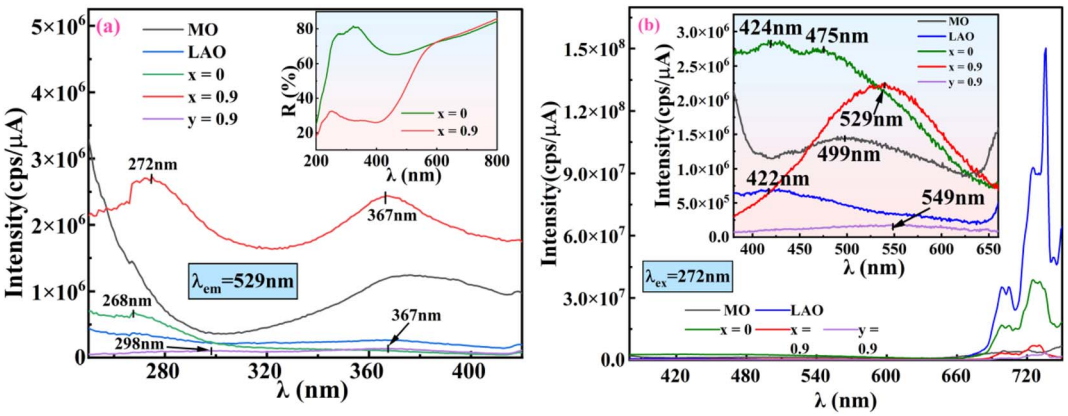

Fig. 7 (a) PLE spectra, (b) PL spectra of MO, LAO, $La_{1-x}Ce_xAlO_3$/MgO (x = 0, 0.9 mol%), $La_{1-y}Ce_yAlO_3$ (y = 0.9 mol%) while the insets of (a) is reflectance *vs.* wavelength (λ) curve for $La_{1-x}Ce_xAlO_3$/MgO (x = 0, 0.9 mol%) and that of (b) is zoomed-in PL spectra of given samples.

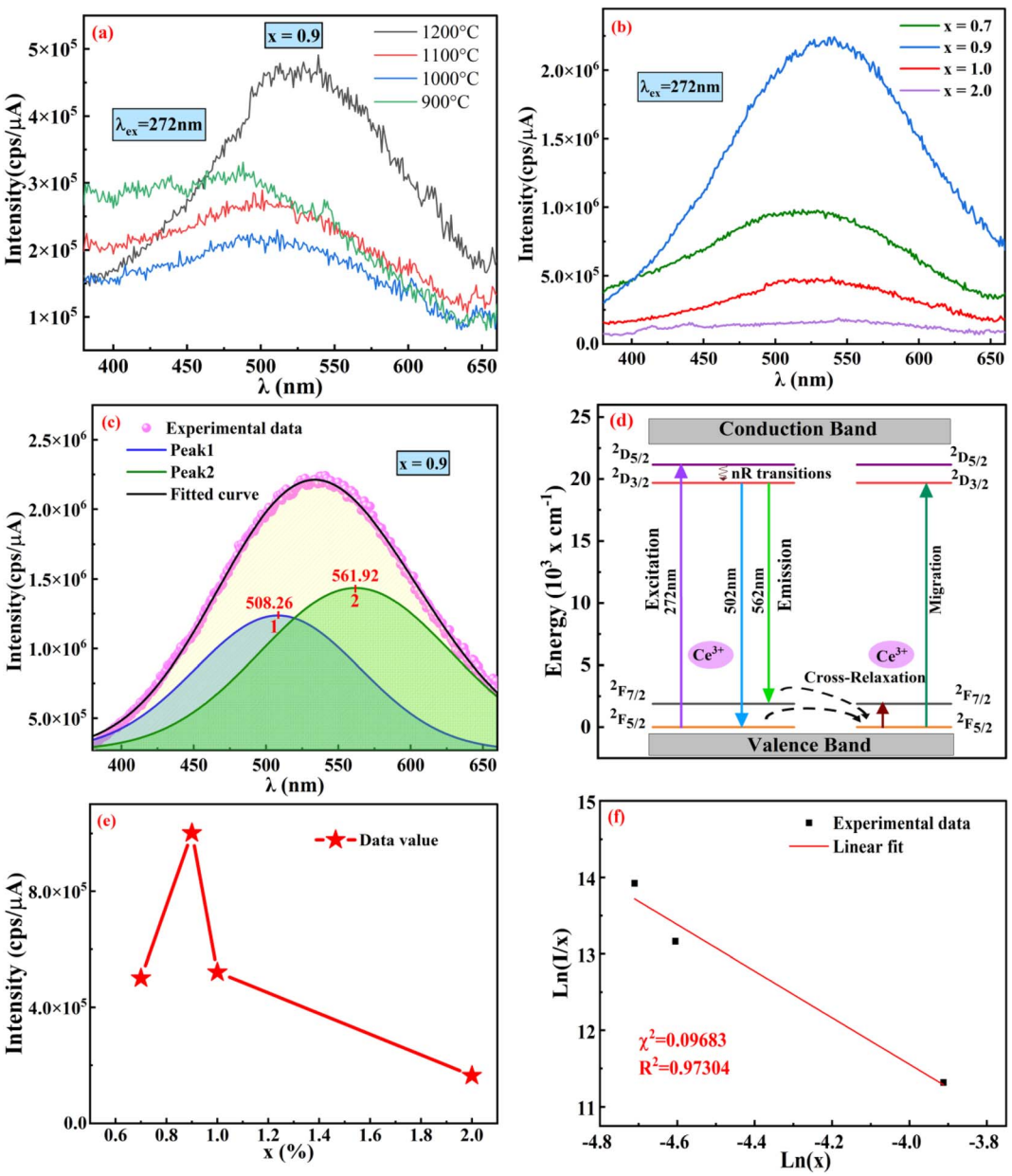

Fig. 8 (a) PL spectra of $La_{1-x}Ce_xAlO_3$/MgO (x = 0.9 mol%) sintered at various temperatures, (b) relative PL spectra *vs.* wavelength (λ) for $La_{1-x}Ce_xAlO_3$/MgO (x = 0, 0.7, 0.9, 1.0, 2.0 mol%), (c) deconvoluted PL spectra of $La_{1-x}Ce_xAlO_3$/MgO (x = 0.9 mol%), (d) schematic energy diagram, (e) relative PL intensities *vs.* dopant concentration (x mol%) and (f) plot of ln(I/x) *vs.* ln(x).

of concentration quenching (CQ) occurring due to non-radiative (nR) energy relocations amongst activator ions. To investigate the valid reason behind CQ, Blasse's (5) has been resolved to calculate the critical distance, R_c (Å) as

$$R_C = 2\left(\frac{3V}{4\pi XN}\right)^{1/3} \quad (5)$$

where V is the volume of unit cell, X is the optimum activator concentration and N is the number of cations to be substituted per unit cell and R_C is the separation between contiguous activator.[52] For R_C < 5 Å, nR energy migration takes place *via* exchange interaction and if it is >5 Å multipolar interactions come into play. For $x = 0.9$ mol% system, $V = 325.225$ Å^3, $X = 0.007$ and $N = 1$, using these R_C has been reckoned to be 44.602 Å which is far larger than 5 Å that indicates nR energy transfer takes place *via* multi-polar interactions. Further, Dexter's theory and Reisfeld's approximation is employed, given by the following relation,

$$\frac{I}{x} = K\left[1 + \beta(x)^{Q/3}\right]^{-1} \quad (6)$$

where, I is the emission intensity and x is the dopant concentration, K and β are constants for given host lattice and Q helps to identify the kind of interaction.[53] Q may take the values 6, 8 and 10 for dipole–dipole (d–d), dipole–quadrupole (d–q) and quadrupole–quadrupole (q–q) multi-photon interaction respectively. Eqn (6) can be simplified as,

$$\log\left(\frac{I}{x}\right) = -\left(\frac{Q}{3}\right)\log(x) + A \quad (7)$$

where A is some constant. Plot of (7) in Fig. 8(f) gives slope $-Q/3$ which in present study yields Q to be 9.142 that is approximately equal to 10, predicting q–q multi-polar interaction to be the underlying plausible mechanism for CQ in Ce^{3+} doped $La_{1-x}Ce_xAlO_3$/MgO phosphors.

4. Time-resolved PL spectroscopy

The PL decay profiles of all the $La_{1-x}Ce_xAlO_3$/MgO (x = 0, 0.7, 0.9, 1.0 and 2.0 mol%) phosphors were recorded for the peak at 562 nm under 272 nm excitation wavelength for 15 ms, which aptly fits bi-exponential function (8) (typical graph for x = 0.9 mol% has been shown in Fig. 9(a)). Estimated lifetimes (τ) using appropriate (9) have been indicated in Table 3.

$$I = I' + A_1\exp\left(-\frac{t}{\tau_1}\right) + A_2\exp\left(-\frac{t}{\tau_2}\right) \quad (8)$$

$$\tau = \frac{A_1\tau_1^2 + A_2\tau_2^2}{A_1\tau_1 + A_2\tau_2} \quad (9)$$

where, I is the emission intensity at time t, τ_1 and τ_2 are two exponential components of τ and I', A_1 and A_2 are fitting parameter constants.[4] With the perusal of calculated data, it is noteworthy that with the rise in rare earth content, measured lifetimes significantly decrease implying energy transfer amongst activator ions. The energy transfer efficiencies (η_T) and probabilities (P) expressed by the (10) and (11) below

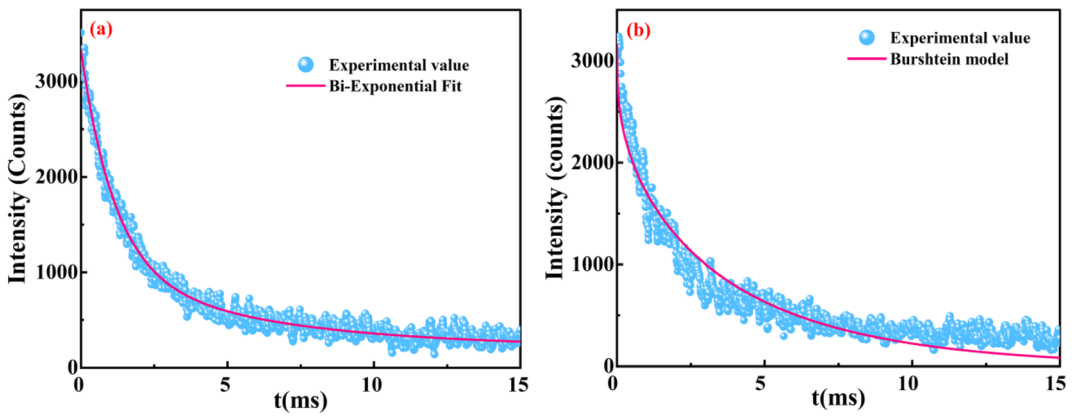

Fig. 9 (a) Bi-exponential fit for $La_{1-x}Ce_xAlO_3$/MgO (x = 0.9 mol%) and (b) Burshtein model fit for $La_{1-x}Ce_xAlO_3$/MgO (x = 1.0 mol%).

Table 3 Detailed TRPL data profiles of $La_{1-x}Ce_xAlO_3$/MgO (x = 0, 0.7, 0.9, 1.0 and 2.0 mol%); τ = life-time, η_T = energy transfer efficiency, P_{nR} = energy transfer probability, S = fitting index, R_0 = critical distance, C_{DA} = donor to acceptor energy transfer rate, W_m = energy migration rate

x (mol%)	τ (ms)	η_T (%)	P_{nR}	S	R_0 (Å)	C_{DA} ($\times 10^{-83}$ m^{10} s^{-1})	W_m ($\times 10^{-19}$ s^{-1})
0	5.763						
0.7	4.676	18.853	0.040	10.86	57.98	745	2.06
0.9	4.084	29.138	0.071	9.40	54.61	409	2.29
1.0	3.852	33.166	0.086	9.45	51.49	227	12.1
2.0	3.776	34.480	0.091	11.67	37.10	8.57	417

$$\eta_T = 1 - \frac{\tau_S}{\tau_{S_0}} \quad (10)$$

$$P = \frac{1}{\tau_S} - \frac{1}{\tau_{S_0}} \quad (11)$$

where, τ_s and τ_{s_0} are the estimated lifetimes of phosphor with and without Ce^{3+} ions.[3,54] The estimated values as mentioned in Table 3 show the rise in both the parameters as the activator concentration goes on increasing. Such trend of decreasing τ and increasing η_T, P with increasing activator content can be attributed to energy transfer between Ce^{3+}–Ce^{3+} ions. This energy transfer may be due to cross-relaxation processes amongst activator ions that may be enhanced with energy migration of excitation energy that can accelerate the decay process. Here, Ce^{3+} ion plays the dual role *i.e.* as donor as well as acceptor ion. The cross-relaxation process involves the exodus of emitting $^2D_{3/2}$ level *via* the transitions $^2D_{3/2}$: $^2F_{5/2} \rightarrow {}^2F_{7/2}$: $^2F_{7/2}$ and $^2D_{3/2}$: $^2F_{5/2} \rightarrow {}^2F_{5/2}$: $^2F_{7/2}$ while energy migration involves the de-population *via* the transitions between neighbouring excited and ground state Ce^{3+} ions through $^2D_{3/2}$: $^2F_{5/2} \rightarrow {}^2F_{7/2}$: $^2D_{3/2}$ transition (Fig. 8(d)).

Standard energy transfer model 'Burshtein model' has been employed to investigate the energy transfer mechanism behind CQ which can be expressed as

$$I(t) = I_0 \times \exp\left[-\frac{t}{\tau_0} - Q \times \left(\frac{t}{\tau_0}\right)^{3/s} - W_m t\right] \quad (12)$$

$$Q = \frac{4\pi}{3} \Gamma\left(1 - \frac{3}{s}\right) N_0 R_0{}^3 \quad (13)$$

$$R_0 = (C_{DA}\tau_0)^{1/s} \quad (14)$$

where, $I(t)$ and I_0 are the emission intensities at time t and initial intensity, τ_0 is the intrinsic decay time of donor ion and Q, S and W_m are the fitting parameters.[55] Respective fitting curve for $La_{1-x}Ce_xAlO_3$/MgO (x = 1.0 mol%) phosphor has been depicted in Fig. 9(b) and calculated fitting parameters have been tabularized in Table 3 for all the doped phosphors. Q is the energy transfer parameter given by (13), where N_0 is the acceptor ion concentration and R_0 is the critical distance between dopant ions at which energy transfer rate to acceptor is equal to the rate of intrinsic decay of donor ion. R_0 is given by (14) in which C_{DA} is the rate of direct energy transfer from donor to acceptor. W_m in (12) is the rate of energy migration among donor ions. S is the index of mechanism involved that can take the values 6, 8 and 10 for d–d, d–q and q–q multi-pole interaction respectively. It is note-worthy from Table 3 that the value of S revolve around 10 implying energy transfer mechanism to be q–q multi-pole interactions supporting the results from PL emission spectra. Also the value of R_0 decreases with increase in dopant concentration which results in better energy transfer efficiencies. For lower concentration of Ce^{3+}, C_{DA} value is much higher and W_m is pretty low while for x = 2.0 mol%, C_{DA} reduces significantly whereas W_m increases by the order of 10^2. This signifies the shift in energy tranfer process from cross-relaxation for lower concentration to energy migration process at higher concentration. Such shifts in mechanism with doping have also been reported earlier in other materials.[56]

5. Band gap determination and chromaticity diagram

Energy band gaps of prepared pristine nano composite, its components, optimized doped nano-composite and its competent *i.e.* $La_{1-y}Ce_yAlO_3$ (y = 0.9 mol%) were calculated *via* Kubelka–Munk equation relating scattering (S), absorption (K) and reflection (R) coefficients as

$$F(R_\infty) = \frac{(1 - R_\infty)^2}{2R_\infty} = \frac{K}{S} = \alpha \quad (15)$$

$$\alpha h\nu = C(h\nu - E_g)^n \quad (16)$$

where h, ν and E_g are Planck's constant, frequency and band gap of the material.[57] Here exponent 'n' can take values 1/2, 3/2, 2, 3 for direct allowed, forbidden, indirect allowed, forbidden transitions respectively. Taking, n = 1/2 for direct allowed transition

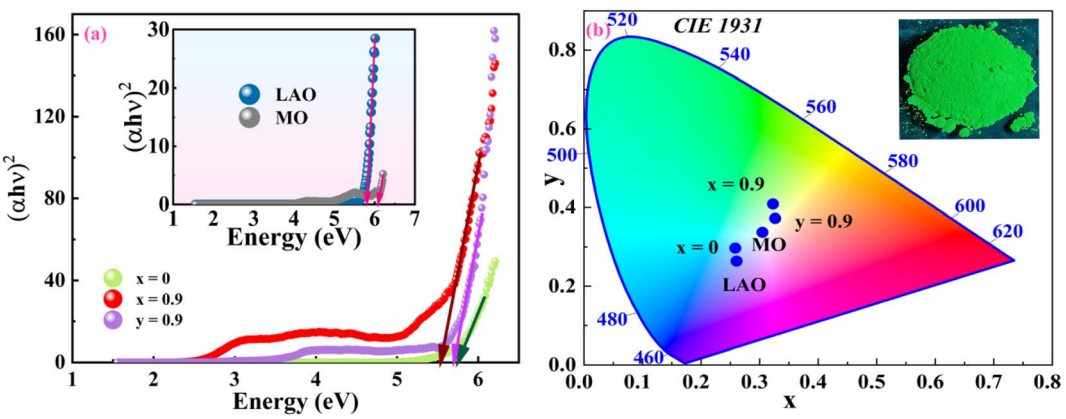

Fig. 10 (a) Tauc plot and (b) CIE-1931 chromaticity diagram for MO, LAO, $La_{1-x}Ce_xAlO_3$/MgO (x = 0 and 0.9 mol%) and $La_{1-y}Ce_yAlO_3$ (y = 0.9 mol%).

Table 4 Optical band gap (E_g), CIE (x, y) coordinates, CCT of MO, LAO, $La_{1-x}Ce_xAlO_3$/MgO (x = 0 and 0.9 mol%) and $La_{1-y}Ce_yAlO_3$ (y = 0.9 mol%)

Sample/x (mol%)/y (mol%)	E_g (eV)	CIE (x, y)	CCT (K)
MO	6.10	(0.30474, 0.33730)	4392
LAO	5.81	(0.26061, 0.26381)	1913
$x = 0$	5.74	(0.25837, 0.29706)	2421
$x = 0.9$	5.53	(0.32270, 0.40902)	5234
$y = 0.9$	5.66	(0.32653, 0.37266)	5316

and calculating band gap by extrapolating tangent drawn to curve in Tauc plot ($(\alpha h\nu)^{1/n}$ *vs.* $h\nu$) (depicted in Fig. 10(a)) and tabulating the results in Table 4.[58] It can be manifested from the tabularized values that both MO and LAO are high band gap semiconductors having E_g 6.10 and 5.81 eV respectively that resemble the earlier reported values.[8,10] Because of large band gap values both are appropriate for host material. Composite of these two, $LaAlO_3$/MgO also show high optical band gap of 5.74, but slightly less than the individual components which may be due to inter-mixing of electronic states of two phases resulting in shifting of valence band and conduction band leading to decreased energy gap.[59] Upon Ce^{3+} doping, E_g of optimized nanophosphor ($La_{1-x}Ce_xAlO_3$/MgO (x = 0.9 mol%)) and $La_{1-y}Ce_yAlO_3$ (y = 0.9 mol%) reduces to 5.53 and 5.66 eV because of extra electronic state occurrence within the host bandgap.[51] But reduction in prepared doped nano-composite is considerably large which results in PL emission wavelength shift relative to individually doped LAO. This justifies the advantage of prepared nano-phosphor composite over individually Ce^{3+} doped LAO.

To identify the color rendering features of generated nano-phosphor powders, color coordinates have been evaluated (tabularized in Table 4) using International Commission of Illumination (CIE) – 1931 color triangle shown in Fig. 10(b). The inset shows the green color luminescence of optimized phosphor under short range UV radiation exposure and similar color is shown in color triangle. Calculated CIE coordinates have been utilized to reckon the coordinated color temperature (CCT) given by the expression given by Mc-Camy as

$$\mathrm{CCT} = 437n^3 + 3601n^2 + 6861n + 5514.31 \quad (17)$$

where $n = (x - x_c)/(y - y_c)$, (x_c, y_c) are chromaticity epicentres having values (0.332, 0.186).[60] CCT values for the samples lie in the range of 1900–5400 K. For CCT < 4000 K, rendered light is said to be warm light and for >5000 K it is called cooled light. This unveils that optimised nanophosphor $La_{1-x}Ce_xAlO_3$/MgO (x = 0.9 mol%) renders cool light which justifies the candidature of prepared nanophosphor for potential applications in w-LEDs, LFP, display devices, scintillation devices, solar cells, *etc.*

6. Application for latent finger printing

Optimized nano-phosphor was utilized for LFP application. Upon visualization of glass slide under 272 nm UV lamp dusted with $La_{1-x}Ce_xAlO_3$/MgO (x = 0.9 mol%) shows several appreciable features of finger pattern. Fig. 11(a) and (b) shows the fingerprint pattern in day light and under UV light respectively. Level 1 coarse feature such as ridge flow pattern, loops and archs are visible in Fig. 11(b). More detailed features like ridge bifurcation, bridge, island and short ridge can be seen in Fig. 11(c)–(f) respectively. Minutest features belonging to level 3, which are hardest to unveil, can also be visualized using this phosphor as sweat pores and dots can be seen in Fig. 11(g) and (h) respectively. This indicates the utility of synthesized phosphor for LFP applications as well as photonic applications.

7. Conclusions

A series of novel cerium doped $La_{1-x}Ce_xAlO_3$/MgO (x = 0, 0.7, 0.9, 1.0 and 2.0 mol%) have successfully been synthesized *via* a robust, low temperature and cost effective synthesis method,

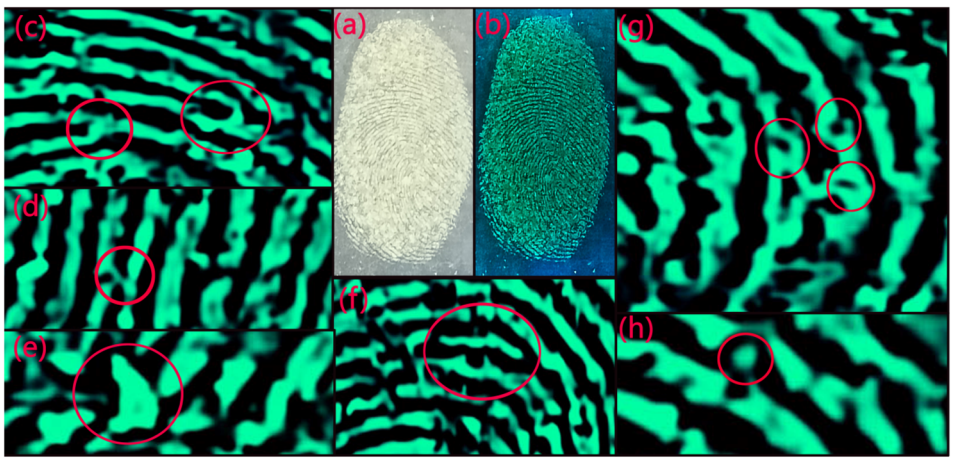

Fig. 11 Fingerprint pattern under (a) day light, (b) 254 nm UV light, zoomed-in images of (b) indicating level 2 and 3 are shown in (c) ridge-bifurcation, (d) bridge, (e) island, (f) short ridge, (g) sweat-pores and (h) dots.

i.e. Pechini sol–gel method. The composite so formed have been found to possess rhombohedral/face-centered structure and emits green color luminescence under UV excitation. The effect of dopant ion concentration on luminescence has been studied which reveals $x = 0.9$ mol% to be the optimum concentration. q–q multipole interaction has been found to be the plausible reason behind CQ. Successful application of optimized phosphors for LFP application suggests it to be the suitable candidate phosphors for photonic as well as imaging applications.

Author contributions

Ashima Makhija: conceptualization, methodology, writing – original draft, Anjli Sharma: methodology, writing – original draft. Sajjan Dahiya: data curation, formal analysis, review. Nisha Deopa: formal analysis, editing. Rajesh Malik: resources, formal analysis. R. Punia: supervision, software. A. S. Maan: resources, validation.

Conflicts of interest

There are no conflicts to declare.

Acknowledgements

Authors would like to convey their heartfelt thanks to UGC, New Delhi, and DST for granting funds under UGC-SAP (F530/5/DRS/2012(SAP-I)) and DST-FIST (SR/FST/PSI-162/2011) to Department of Physics, MDU Rohtak. One of the authors, Ashima Makhija acknowledges Maharshi Dayanand University, Rohtak for the financial aid by the award of URS (No. R&S/R-12/22/URS/5023).

References

1 J. Dwivedi, P. Kumar, A. Kumar, Sudama, V. N. Singh, B. P. Singh, S. K. Dhawan, V. Shanker and B. K. Gupta, *RSC Adv.*, 2014, **4**, 54936–54947.
2 M. K. Sahu, M. Jayasimhadri, K. Jha, B. Sivaiah, A. S. Rao and D. Haranath, *J. Lumin.*, 2018, **202**, 475–483.
3 P. Sehrawat, R. K. Malik, P. Boora, M. Punia, M. Sheoran, P. Chhillar, S. P. Khatkar and V. B. Taxak, *Chem. Phys. Lett.*, 2021, **763**, 138243.
4 R. Lohan, A. Kumar, M. K. Sahu, A. Mor, V. Kumar, N. Deopa and A. S. Rao, *J. Mater. Sci.: Mater. Electron.*, 2023, **34**(8), DOI: 10.1007/s10854-023-10055-z.
5 S. Kaur, A. S. Rao, M. Jayasimhadri, B. Sivaiah and D. Haranath, *J. Alloys Compd.*, 2019, **802**, 129–138.
6 M. A. Farrukh, K. M. Butt, K. K. Chong and W. S. Chang, *J. Saudi Chem. Soc.*, 2019, **23**, 561–575.
7 Z. Liu, L. Sinatra, M. Lutfullin, Y. P. Ivanov, G. Divitini, L. De Trizio and L. Manna, *Adv. Energy Mater.*, 2022, **12**(38), 2201948.
8 T. Manohar, S. C. Prashantha, R. Naik, H. Nagabhushana, H. P. Nagaswarupa, K. S. Anantharaju, K. M. Girish and H. B. Premkumar, *Sens. Actuators, B*, 2017, **243**, 1057–1066.
9 N. Badar, N. F. Chayed, R. Rusdi, N. Kamarudin and N. Kamarulzaman, *Adv. Mater. Res.*, 2012, **545**, 157–160.
10 C. Nor Fadilah, K. Norlida, B. Nurhanna and E. Kelimah, *Solid State Phenom.*, 2019, **290**, 323–328.
11 M. Sheoran, P. Sehrawat, N. Kumari, M. Kumar and R. K. Malik, *Chem. Phys. Impact*, 2022, **4**, 100063.
12 S. K. Baghel, N. Brahme, D. P. Bisen, Y. Patle, T. Richhariya, E. Chandrawanshi and C. Belodhiya, *Opt. Mater.*, 2022, **126**, 112141.
13 G. J. Jeong, T. W. Kang, Y. J. Park, Y. J. Park, Y. Lee, B. Bae and S. W. Kim, *RSC Adv.*, 2021, **11**, 24949–24957.
14 T. Richhariya, N. Brahme, D. P. Bisen, T. Badapanda, K. Tiwari and A. Jain, *Mater. Sci. Semicond. Process.*, 2023, **159**, 107396.
15 G. Dantelle, D. Testemale, E. Homeyer, A. Cantarano, S. Kodjikian, C. Dujardin, J.-L. Hazemann and A. Ibanez, *RSC Adv.*, 2018, **8**, 26857–26870.
16 T. Kang, S. Lim, S. Lee, H. Kang, Y. Yu and J. Kim, *Opt. Mater.*, 2019, **98**, 109501.
17 J. Chan, L. Cao, W. Li, N. Ma, Z. Xu and X. Huang, *Inorg. Chem.*, 2022, **61**, 6953–6963.
18 B. Evangeline, P. A. Azeem, R. Prasada Rao, G. Swati and D. Haranath, *J. Alloys Compd.*, 2017, **705**, 618–623.
19 X. D. Wang, T. Pan, T. C. Zang, J. K. Li, Z. W. Zhao, L. H. Zhang and J. Xu, *Sci. China, Ser. E: Technol. Sci.*, 2009, **52**, 3678–3682.
20 T. Manohar, S. C. Prashantha, H. Nagabhushana, K. Channakeshavalu and H. P. Nagaswarupa, *Mater. Today: Proc.*, 2017, **4**, 11848–11856.
21 Yashaswini, S. Pratibha, R. Lokesh, N. Dhananjaya and C. Pandurangappa, *Inorg. Chem. Commun.*, 2023, **34**(8), 108342.
22 R. Shi, L. Yu, Y. Tian, X. Wang, Z. Sun, B. Qi and F. Luo, *Mater. Chem. Phys.*, 2022, **280**, 1–10.
23 K. Si-ahmed and Y. Bessekhouad, *Mater. Today Commun.*, 2022, **31**, 103450.
24 D. Navami, G. P. Darshan, D. R. Lavanya, H. B. Premkumar, S. C. Sharma, H. Adarsha, H. C. Prameela and H. Nagabhushana, *Opt. Mater.*, 2021, **122**, 111474.
25 C. R. Garcia, J. Oliva and L. A. Diaz-torres, *Ceram. Int.*, 2021, **47**, 10–41.
26 J. Carvajal, *Acta Crystallogr.*, 1967, **22**, 151.
27 H. M. Rietveld, *J. Appl. Crystallogr.*, 1969, **2**, 65–71.
28 K. Momma and F. Izumi, *J. Appl. Crystallogr.*, 2011, **44**, 1272–1276.
29 X. Dong, X. Cui, Z. Fu, S. Zhou, S. Zhang and Z. Dai, *Mater. Res. Bull.*, 2012, **47**, 212–216.
30 A. B. S. Garcia, A. G. Bispo Jr, S. A. M. Lima and A. M. Pires, *Mater. Res. Bull.*, 2021, **143**, 111462.
31 S. Ghorbani, R. S. Razavi, M. R. Loghman-Estarki and A. Alhaji, *J. Cluster Sci.*, 2017, **28**, 1523–1539.
32 I. S. Silveira, N. S. Ferreira and D. N. Souza, *Ceram. Int.*, 2021, **47**, 27748–27758.
33 P. Kumar, S. Singh, I. Gupta, V. Kumar and D. Singh, *Inorg. Chem. Commun.*, 2022, **141**, 109578.
34 D. Singh, J. Kaur, N. S. Suryanarayana, R. Shrivastava and V. Dubey, *J. Mater. Sci.: Mater. Electron.*, 2017, **28**, 2462–2470.

35 M. Beheshti and R. Malekfar, *Mater. Chem. Phys.*, 2021, **270**, 124848.
36 S. Kozuka, J. Ueda and S. Tanabe, *Phys. B*, 2022, **633**, 413492.
37 P. Ankoji and B. Hemalatha Rudramadevi, *Opt. Mater.*, 2019, **95**, 109249.
38 E. B. Shaik, B. V. N. Kumar, S. K. Chirauri and K. R. Rao, *J. Mater. Sci.: Mater. Electron.*, 2022, **33**, 105–114.
39 M. Rizwan, S. Gul, T. Iqbal, U. Mushtaq, M. H. Farooq, M. Farman, R. Bibi and M. Ijaz, *Mater. Res. Express*, 2019, **6**(11), 112001.
40 P. Sharma, N. Berwal, N. Ahlawat, A. S. Maan and R. Punia, *Ceram. Int.*, 2019, **45**, 20368–20378.
41 W. Hume-Rothery, *J. Inst. Met.*, 1926, **35**, 295–361.
42 P. Debye and P. Scherrer, *Phys. Z.*, 1916, **17**, 277–283.
43 W. Hall and G. K. Williamson, *Acta Metall.*, 1953, **1**, 22–31.
44 R. H. Krishna, B. M. Nagabhushana, H. Nagabhushana, N. S. Murthy, S. C. Sharma, C. Shivakumara and R. P. S. Chakradhar, *J. Phys. Chem. C*, 2013, **117**, 1915–1924.
45 B. D. Cullity, *Elements of X-ray Diffraction*, Addison-Wesley Publishing, 1956.
46 N. Siedl, D. Koller, A. K. Sternig, D. Thomele and O. Diwald, *Phys. Chem. Chem. Phys.*, 2014, **16**, 8339–8345.
47 N. I. Mukhurov, S. P. Zhvavyi, I. V. Gasenkova, S. N. Terekhov, P. P. Pershukevich and V. A. Orlovich, *J. Appl. Spectrosc.*, 2010, **77**, 591–597.
48 J. Q. Chen, X. Wang, Y. H. Lu, A. Roy Barman, G. J. You, G. C. Xing, T. C. Sum, S. Dhar, Y. P. Feng, Ariando, Q. H. Xu and T. Venkatesan, *Appl. Phys. Lett.*, 2011, **98**, 1–4.
49 P. B. Devaraja, D. N. Avadhani, S. C. Prashantha, H. Nagabhushana, S. C. Sharma, B. M. Nagabhushana and H. P. Nagaswarupa, *Spectrochim. Acta, Part A*, 2014, **118**, 847–851.
50 S. Agarwal, M. S. Haseman, A. Khamehchi, P. Saadatkia, D. J. Winarski and F. A. Selim, *Opt. Mater. Express*, 2017, **7**, 1055.
51 H. Dalal, M. Kumar, P. Sehrawat, M. Sheoran, N. Sehrawat, S. Kumar and R. K. Malik, *J. Mater. Sci.: Mater. Electron.*, 2022, **33**, 13743–13756.
52 G. Blasse, *Philips Res. Rep.*, 1969, **24**, 131.
53 D. L. Dexter, *J. Chem. Phys.*, 1953, **21**, 836–850.
54 S. Kaur, A. S. Rao and M. Jayasimhadri, *Mater. Res. Bull.*, 2019, **116**, 79–88.
55 A. D. Sontakke, K. Biswas, A. K. Mandal and K. Annapurna, *Appl. Phys. B: Lasers Opt.*, 2010, **101**, 235–244.
56 G. Gupta, S. Balaji, K. Biswas and K. Annapurna, *AIP Adv.*, 2019, **9**(4), 045201.
57 R. Punia, R. S. Kundu, J. Hooda, S. Dhankhar, S. Dahiya and N. Kishore, *J. Appl. Phys.*, 2011, **110**(3), 033527.
58 J. Tauc, *Mater. Res. Bull.*, 1970, **5**, 721–729.
59 H. M. Shanshool, M. Yahaya, W. M. M. Yunus and I. Y. Abdullah, *J. Mater. Sci.: Mater. Electron.*, 2016, **27**, 9804–9811.
60 C. S. McCamy, *Color Res. Appl.*, 1992, **17**, 142–144.